

Article

Evolution of Nanodomains and Formation of Self-Organized Structures during Local Switching in X-Cut LNOI

Boris Slautin , Anton Turygin , Elena Pashnina, Alla Slautina , Dmitry Chezganov  and Vladimir Shur * 

School of Natural Science and Mathematics, Ural Federal University, 620000 Ekaterinburg, Russia; boris.slautin@urfu.ru (B.S.); anton.turygin@urfu.ru (A.T.); elena.pashnina@urfu.ru (E.P.); alla.slautina@urfu.ru (A.S.); chezganov.dmitry@urfu.ru (D.C.)

* Correspondence: vladimir.shur@urfu.ru

Abstract: The features of nanodomain growth during local switching in X-cut lithium niobate on insulator (LNOI) were comprehensively studied using the biased tip of a scanning probe microscope. The obtained results were discussed in terms of the kinetic approach. The revealed differences in domain growth in bulk LN and LNOI were attributed to the higher bulk conductivity of LNOI. The obtained influence of humidity on the shape and growth of isolated domains was attributed to the water meniscus. Analysis of the transition between the “forward growth” and “sideways growth” stages was performed by switching to the stripe electrode. A sand-glass-shaped domain was formed due to growth in the opposite direction after the domain touched the electrode. Stable periodical domain structures down to 300 nm were created and characterized in LNOI. Highly ordered comb-like domains of various alternating lengths, including four- and eight-fold increase periods, were produced by performing biased tip scanning along the Y axis. The obtained knowledge is important for the future development of nanodomain engineering methods in monocrystalline ferroelectric thin films on insulators.



Citation: Slautin, B.; Turygin, A.; Pashnina, E.; Slautina, A.; Chezganov, D.; Shur, V. Evolution of Nanodomains and Formation of Self-Organized Structures during Local Switching in X-Cut LNOI. *Crystals* **2022**, *12*, 659. <https://doi.org/10.3390/cryst12050659>

Academic Editors: Tzi-yi Wu and Ali Belarouci

Received: 18 April 2022

Accepted: 2 May 2022

Published: 5 May 2022

Publisher's Note: MDPI stays neutral with regard to jurisdictional claims in published maps and institutional affiliations.



Copyright: © 2022 by the authors. Licensee MDPI, Basel, Switzerland. This article is an open access article distributed under the terms and conditions of the Creative Commons Attribution (CC BY) license (<https://creativecommons.org/licenses/by/4.0/>).

Keywords: lithium niobate; domain structure; local switching; non-polar cut; self-organization; nanodomain engineering; forward growth

1. Introduction

Lithium niobate on insulator (LNOI) wafers are among the most promising materials for various integrated optical and acoustic devices [1–3]. LNOI wafers usually consist of an ion-sliced monocrystalline lithium niobate (LN) film, with a thickness of 300–900 nm, attached to the SiO₂ layer on the LN substrate [4]. This structure allows the basic advantages of LN, namely, the wide spectral transparency window, large electro-optic coefficient, and strong second-order nonlinearity, to be combined with the small thickness and strong drop in refractive index on the LN/SiO₂ interface ($\Delta n \approx 0.67$) [5,6]. Therefore, LNOI is extremely attractive for quantum photonic and non-linear optics. The realization of low-loss waveguides [7–11], high-speed electro- and acousto-optic modulators [1,3,5,12,13], non-linear frequency converters [14,15], micro-disk and micro-ring resonators [16–19], and grating couplers [20–22] has been demonstrated recently.

It is known that the creation of stable periodical domain structures with nanoscale period reproducibility (periodical poling) can improve the efficiency of light frequency conversion by producing a quasi-phase matching (QPM) effect [23–25]. Numerous prototypes of very efficient wavelength converters, including second harmonic generators (SHGs), sum-frequency generators (SFGs), and difference frequency generators (DFGs) [14,15,26–28], have already been demonstrated. Particular attention has been paid to the production of periodically poled LNOI (PPLNOI) with submicron periods, to enable backward optical harmonic generation, which could be used to create a mirrorless optical parametric oscillator (MOPO) [29]. The production of PPLNOI with submicron periods remains a challenging

task, due to domain–domain interactions and backswitching in LN crystals. The creation of periodical domain structures down to 200 nm in Z-cut LNOI using the biased tip of a scanning probe microscope (SPM) [30,31] has been reported recently.

Nowadays, SPM is successfully used in LNOI wafers to create domain structures and domain imaging using piezoelectric force microscopy (PFM) [32–37]. Investigations have primarily been performed on Z-cut LNOI. Periodical poling in X-cut LNOI has been realized using lithographically produced electrodes with a minimal period of 600 nm [15,26,38]. However, the creation of domain structures with lower periods in X-cut LNOI, which are attractive for applications, has still not been studied.

This paper is devoted to an investigation of the formation of domain structures during local switching in X-cut LNOI. The study of the growth, interaction, and stability of isolated nanodomains and periodical domain structures facilitated the creation of X-cut PPLNOI with a submicron period. The formation of self-organized nanoscale domain structures was revealed and discussed.

2. Materials and Methods

The studied X-cut LNOI wafers (LN film/SiO₂/LN substrate) were provided by Jinan Jingzheng Electronics (NanoLN, Jinan, China). The thicknesses of different layers of the wafer were as follows: LN film—300 nm; SiO₂ layer—1 μm; LN substrate—500 μm. Domain growth in LN thin film and bulk X-cut LN crystal with a thickness of 500 μm was compared. The surface roughness of both samples was below 1 nm.

The scanning probe microscope Ntegra Aura (NT-MDT, Zelenograd, Russia) was used for domain creation and imaging. The isolated domains were created using local switching by single DC pulses with an amplitude of 50 to 300 V and duration of 10 ms to 100 s (Figure 1a). Comb-like domains were formed by scanning using a biased tip along the Z axis (Figure 1c). Moreover, we studied the domain growth towards the Pt 30 nm-thick and 200 μm-wide stripe electrode deposited by magnetron sputtering and oriented along the Y axis (Figure 1b). The electrode pattern was produced using electron beam lithography by the “lift-off” process. All the measurements were carried out in a nitrogen atmosphere with relative humidity (RH), controlled by an internal sensor in SPM, with an accuracy of about 1%.

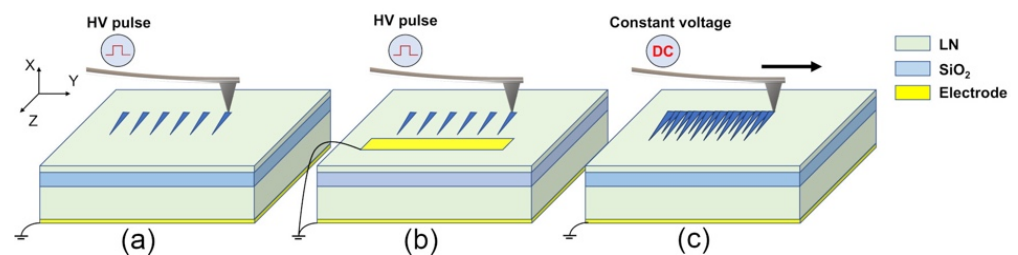


Figure 1. Schemes of the poling setups for (a) isolated domains and periodical poling, (b) domain switching toward the stripe electrode, and (c) creation of comb-like domains.

Domain imaging was carried out using PFM and an electron channeling method (ECM). We used single-frequency PFM with a voltage amplitude of 3–6 V and a frequency far from the resonance. PFM collects the piezoelectric signal from a depth of hundreds of nanometers [39]. The ECM is based on the change in intensity of the back-scattered electrons, depending on the crystallographic structure of the sample [40]. The high sensitivity of ECM to the surface crystallographic structure facilitates ferroelectric domain imaging in the layer with a depth of tens of nanometers [41–43]. The ECM was performed with an EVO-LS10 scanning electron microscope (Carl Zeiss NTS, Jena, Germany) using an angle-selected, four-quadrant, back-scattered electron detector.

3. Results and Discussion

3.1. Isolated Domains

The growth of the isolated domains in the polar direction, under local switching, was studied in an X-cut bulk crystal and a thin film. The domains were created by rectangular pulses with voltages ranging from 75 to 200 V and a 5 s duration at an RH of 30%. The dependence of the domain shape on the pulse polarity was analyzed.

In the LNOI film, the application of negative pulses led to the formation of wedge-like domains, whereas the application of positive pulses led to the appearance of domains with several “spikes” (Figure 2a). The number of “spikes” decreased with the pulse amplitude. In the bulk LN crystals, long narrow domains were formed after the application of negative pulses, whereas wedge-like domains appeared after the application of positive pulses (Figure 2b). The linear voltage dependence of the domain length obtained for both pulse polarities is typical for switching in LN (Figure 2c,f) [44]. The voltage dependences of the domain base width (w) for both pulse polarities in LNOI (Figure 2d) and for positive pulses in bulk LN (Figure 2g) were successfully fitted by $w(U) = a(U - U_{th})^{1/2}$, determined from the spatial distribution of the field polar component near the tip–surface contact [44], where a is the constant and U_{th} is the threshold voltage for domain nucleation. In contrast, the width of the domains created by negative pulses in bulk LN remained constant in the entire voltage range. The best-fit values of the threshold voltages were about 25 V for LNOI and 35 V for bulk LN.

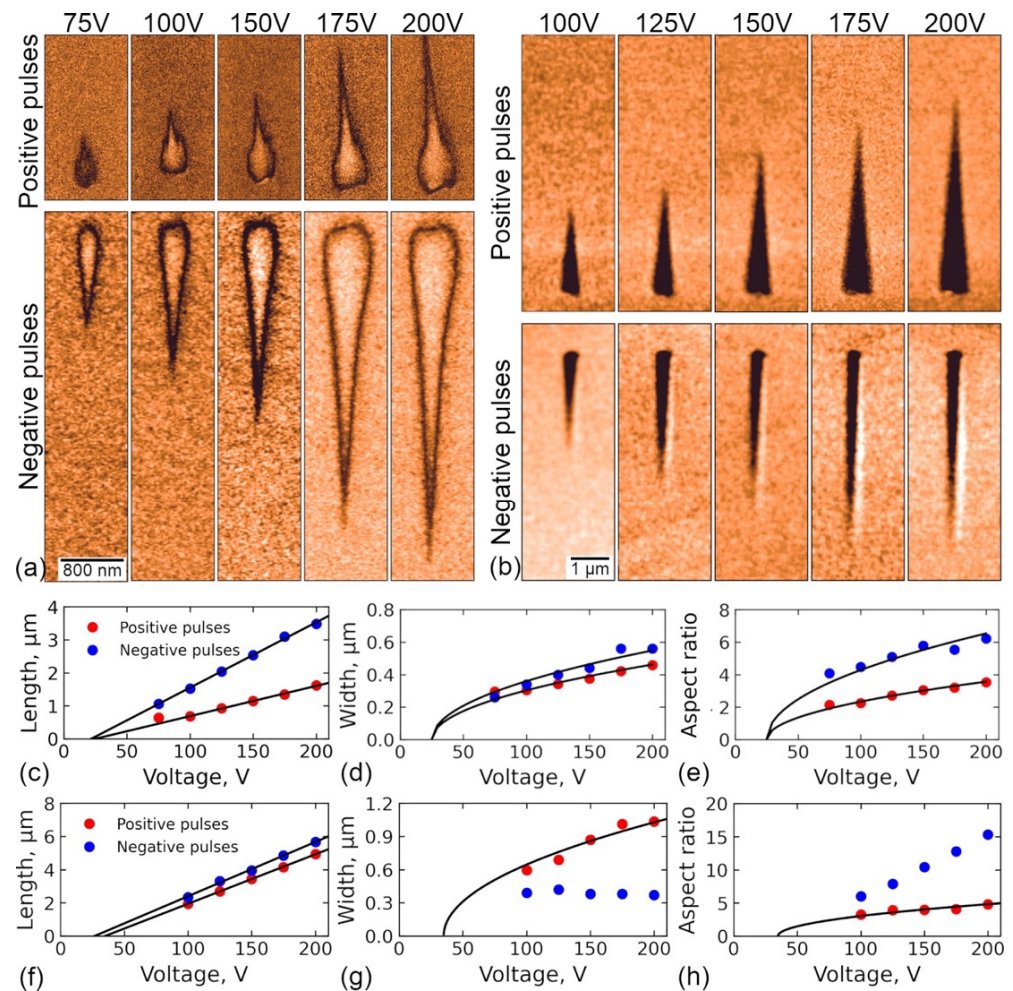


Figure 2. PFM images of isolated domains created in (a) LNOI and (b) bulk LN by positive and negative voltage pulses. The voltage dependences of the domain (c,f) length, (d,g) width, and (e,h) aspect ratio in (c–e) LNOI and (f–h) bulk LN. The pulse duration was 5 s.

For an explanation of the obtained difference in the domain shape and voltage dependences of the domain sizes between the bulk crystal and LNOI, the domain growth was considered in terms of the kinetic approach [44]. According to the kinetic approach, domain growth occurs under the polar component of an electric field (E_{loc-z}) by generating the elementary steps with charged kinks and kink motion along the wall. E_{loc-z} represents the sum of the external field applied by the tip (E_{ex-z}), the local depolarization field (E_{dep-z}), and the screening field (E_{scr-z}).

$$E_{loc-z}(r, t) = E_{ex-z}(r, t) - E_{dep-z}(r, t) + E_{scr-z}(r, t) \quad (1)$$

Step generation occurs at the domain base in the vicinity of the tip, under the action of E_{ex-z} . It is close to zero at a distance of around one micron from the tip.

Domain elongation (forward growth) is caused by partially screened E_{dep-z} produced far from the domain base by charged kinks, which stimulates kink motion. The screening field E_{scr-z} slows down the kink motion and prevents spontaneous backswitching after pulse termination.

$$E_{loc-z}(r, t) = E_{dep-z}(r, t) - E_{scr-z}(r, t) \quad (2)$$

The screening effectiveness depends on the conductivity of the charged domain walls (CDWs) of the wedge-like domains and bulk conductivity. It is necessary to take into account that the “head-to-head” CDWs that appeared after the application of the positive pulse possess at least an order of magnitude higher conductivity than the “tail-to-tail” CDWs that appeared after the application of the negative pulse [45,46]. Moreover, the conductivity in LNOI (10^{-13} Sm/mm) is about five orders of magnitude higher than that in bulk crystals [47,48], due to the point defects induced by ion irradiation and incompletely removed by annealing.

In bulk LN, formation of the stable wedge-like domain under the positive pulses can be attributed to the high conductivity of the “head-to-head” CDWs, which provide effective screening and, thus, prevent backswitching.

In LNOI, more effective screening, caused by high bulk conductivity, diminishes the field produced by kinks. This results in a decrease in the domain elongation by kink motion and an increase in the CDW tilt, which leads to the formation of additional narrow “spikes” [49].

Formation of the narrow wedge-like domains under negative pulses in bulk LN can be attributed to the pronounced backswitching effect, caused by the low conductivity of “tail-to-tail” CDWs. In this case, the domain width determined by the interaction of approaching walls is independent of the applied voltage.

Domains created in LNOI by negative pulses have low conductive “tail-to-tail” CDWs, which leads to the growth of long wedge-like domains. At the same time, the high bulk conductivity prevents backswitching and the width of the created wedge-like domain persists after pulse termination.

The influence of humidity on domain growth was studied at an RH ranging from 20% to 70%, with pulses of -125 V to -200 V and a duration of 1 s (Figure 3). Three RH regions, characterized by different domain shapes, were distinguished.

For low humidity ($RH < 45\%$), the length of the wedge-like domains is almost independent of RH, whereas the significant increase in the domain width leads to a decrease in the aspect ratio (Figure 3b–d).

For moderate humidity ($45\% < RH < 60\%$), the formation of domains with a wide base and narrow tail was observed. The base width was almost independent of RH, whereas the base length slightly decreased (Figure 3c,d).

For high humidity ($RH > 60\%$), the base width decreased significantly with RH and the domain length continued to decrease (Figure 3c,d); thus, the aspect ratio increased significantly (Figure 3b).

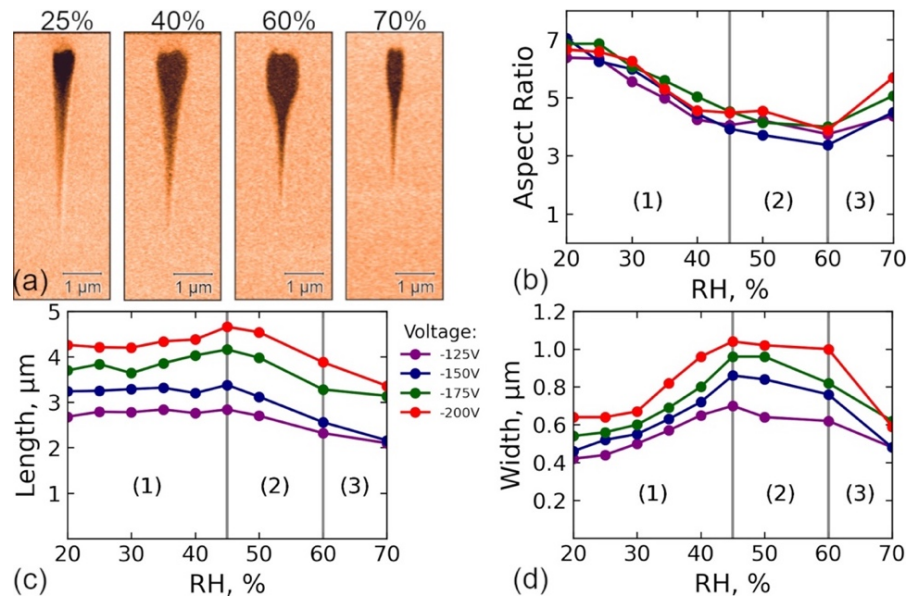


Figure 3. (a) PFM images of isolated domains for various RH at a voltage of -200 V. Dependence of the (b) aspect ratio, (c) length, and (d) width on RH for various voltages. The pulse duration was 1 s.

Domain shape transformation with RH can be attributed to the formation and growth of a water meniscus in the tip–surface contact [50]. The appearance of the small meniscus at $\text{RH} < 45\%$ led to the delocalization of $E_{\text{ex-z}}$ and an increase in the domain width. The continuous growth of the meniscus at a moderated RH improved the screening of $E_{\text{dep-z}}$, which led to the formation of a domain with a wide base and narrow tail. The decrease in domain width at a high RH was attributed to the significant diminishing of $E_{\text{ex-z}}$, due to strong delocalization.

The domain growth towards the stripe electrode was studied for switching using pulses with various voltages and durations at an RH of 30% (Figure 4a–d). The biased tip was placed 4 μm from the grounded stripe electrode. The nonuniform domain contrast in the PFM (Figure 4a,b) and ECM (Figure 4c,d) images allowed the local domain depth to be qualitatively characterized and the domain growth to be restructured. The darker regions correspond to the deeper domain.

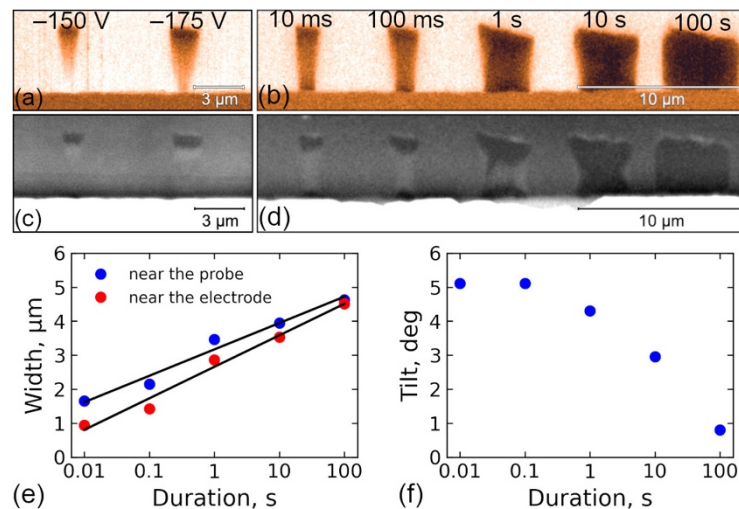


Figure 4. Domain growth toward the grounded stripe electrode. (a,b) PFM and (c,d) SEM images of domains created by pulses with various (a,c) voltages (pulse duration 1 s) and (b,d) pulse durations (voltage was -175 V). Dependences of the (e) domain width and (f) domain wall tilt on pulse duration.

The wedge-like domains with CDWs started to grow towards the electrode. After the domain had touched the electrode, the domain growth from the electrode towards the tip led to the formation of “head-to-head” CDWs, thus creating a sand-glass-shaped domain. The subsequent growth promoted its rapid transformation to the stripe domain with a neutral domain wall. The obtained results allowed the transition between the main stages of the domain evolution—from “forward growth” to “sideways growth”—to be observed [51].

3.2. Periodical Domain Structures

Arrays of isolated domains with various periods were created to investigate domain–domain interactions. Domain length alternation in arrays with small periods had already been demonstrated on polar and nonpolar cuts of bulk LN [52,53]. A decrease in the period leads to intermittent quasiperiodic and chaotic behavior. This effect has never been observed in Z-cut LNOI [33].

We obtained a uniform domain length for the entire range of periods from 4 to 0.3 μm (Figure 5a–c). The width of the domain increased over the period, while the aspect ratio essentially decreased from 25 to 7 (Figure 5e,f). The domain length increased linearly with voltage (Figure 5g). The variation in domain lengths was obtained for the 300 nm period, switched at voltages above -200 V (Figure 5d,g). It is necessary to point out that the achieved domain length above 3 μm is sufficient for LN waveguides with a width of around 1 μm .

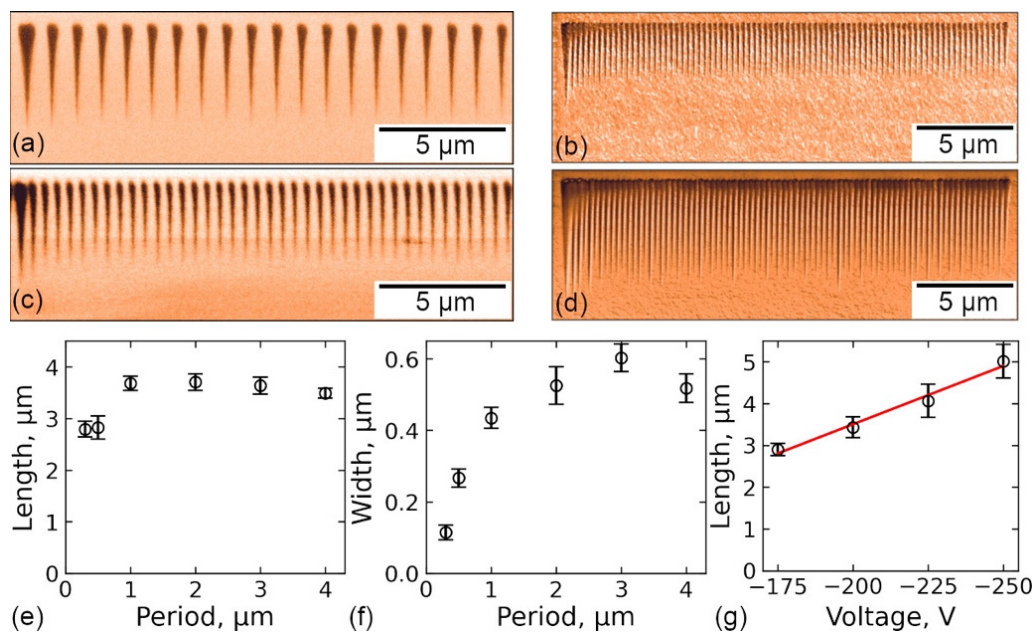


Figure 5. PFM images of domain arrays with periods: (a) 1 μm and (c) 500 nm. PFM images of domain arrays with a period of 300 nm switched by (b) -175 V and (d) -250 V. Dependences on the period of domain (e) length and (f) base width. (g) Dependence of domain length on voltage.

3.3. Self-Organized Domain Structures

The self-organized domain structures were formed during scanning with a biased tip along the Y axis with a voltage of -175 V and scanning rate of 5 $\mu\text{m}/\text{s}$ at various levels of RH (Figure 6). The strongly pronounced dependence of the domain structure on RH was revealed. Only a few isolated narrow domains appeared in dry nitrogen and at an RH of 60% (Figure 6a,c). Self-organized “comb-like” structures, consisting of narrow domains, were formed at a humidity of around 25% (Figure 6b). A similar effect had been previously obtained on nonpolar cuts of bulk LN [54].

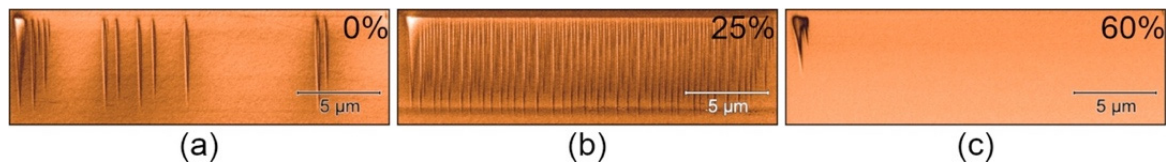


Figure 6. PFM domain images: scanning with a voltage of -175 V and a rate of $5 \mu\text{m/s}$ at an RH of (a) 0%, (b) 25%, and (c) 60%.

The effect of self-organization can be clearly observed in a histogram (Figure 7e) and Poincaré plot, which represents the dependence of the length of each domain in the array on the length of its neighbor (Figure 7f). An analysis of the Poincaré plot revealed the formation of six separated clusters, corresponding to four groups of domains, which can also be clearly distinguished in the histogram: L—large; M—medium; S—short; and T—tiny. The formation of quasiperiodic alternations of domain length, such as four- (L-T-S-T-...) (Figure 7b) and eight-fold (L-T-S-T-M-T-S-T...) period increases (Figure 7c), was observed. Arrays with chaotic alternation were also obtained (Figure 7d).

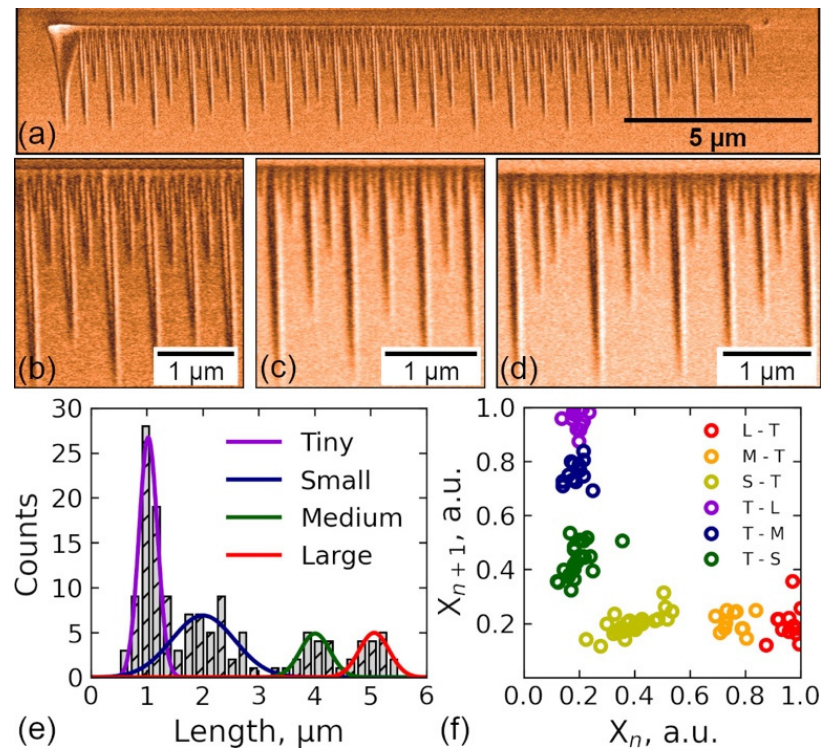


Figure 7. PFM images of self-organized domain structures: (a) general view, (b) four-fold period increases, (c) eight-fold period increases, and (d) chaotic period. (e) Bar chart of the domain length. (f) Poincaré plot: RH, 30%; scanning rate, $5 \mu\text{m/s}$; voltage, -175 V.

The self-organization was attributed to the electrostatic interaction between neighboring domains in the array, where large (L) or medium (M) domains suppressed the growth of the neighboring domains and led to the formation of tiny (T) and small (S) domains. It should be noted that only quadruple- and double-length periods had been previously observed in the bulk LN [53]; the eight-fold increase in the periods was observed for the first time in the current study.

The obtained knowledge is important for the future development of domain engineering methods in monocrystalline ferroelectric thin films on insulators. It forms the basis for the implementation of periodical domain patterning in mass production by local switching on X-cut thin films using lithographically produced electrodes with submicron periods.

4. Conclusions

A comprehensive investigation of the features of domain growth during local switching in X-cut LNOI, using the biased tip of a scanning probe microscope, was performed. The obtained results have been discussed in terms of the kinetic approach. The revealed differences in domain growth in bulk LN and LNOI are attributed to the unusual screening of the depolarization field, caused by the high bulk conductivity of LNOI. The obtained significant influence of humidity on the shape and growth of isolated domains in LNOI is attributed to the formation of the water meniscus.

The transition between the main stages of the domain evolution—“forward growth” and “sideways growth”—was performed by local switching toward the stripe electrode in LNOI. It was shown that after the domain had touched the electrode, the growth in the opposite direction from the electrode toward the tip led to the formation of a sand-glass-shaped domain. The subsequent domain growth promoted its rapid transformation to the stripe domain with neutral walls.

It was shown that weak domain–domain interactions enabled the creation of periodical domain structures with submicron periods in LNOI. Stable periodical domain structures with periods down to 300 nm were created and characterized, which are essentially lower than those achieved using lithographically produced electrodes [15,26,38].

Highly ordered comb-like domains of various alternating lengths, including four- and eight-fold increases in periods, were produced using biased tip scanning along the Y axis.

The obtained knowledge is important for the future development of domain engineering methods in monocrystalline ferroelectric thin films on insulators. It forms the basis for the implementation of periodical domain patterning by local switching on X-cut thin films using lithographically produced electrodes with submicron periods.

Author Contributions: Conceptualization, B.S. and V.S.; resources, E.P. and D.C.; investigation, B.S. and A.S.; supervision, B.S., A.T. and V.S.; writing—original draft preparation, B.S.; writing—review and editing, V.S. All authors have read and agreed to the published version of the manuscript.

Funding: This research was funded by RFBR and Government of Sverdlovsk region (Project No. 20-42-660025), by the Ministry of Science and Higher Education of the Russian Federation (projects 075-15-2021-677).

Data Availability Statement: The data that support the findings of this study are available from the corresponding author upon reasonable request.

Acknowledgments: The equipment of the Ural Center for Shared Use “Modern nanotechnology” Ural Federal University (Reg. No. 2968) was used. The authors thank Huabin Zhu, Jinan Jingzheng Electronics Co. Ltd., for his invaluable help in providing LNOI samples.

Conflicts of Interest: The authors declare no conflict of interest. The founding sponsors had no role in the design of the study; in the collection, analyses, or interpretation of the data; in the writing of the manuscript; or in the decision to publish the results.

References

1. Poberaj, G.; Hu, H.; Sohler, W.; Gunter, P. Lithium niobate on insulator (LNOI) for micro-photonics devices. *Laser Photon. Rev.* **2012**, *6*, 488–503. [[CrossRef](#)]
2. Hu, H.; Yang, J.; Gui, L.; Sohler, W. Lithium niobate-on-insulator (LNOI): Status and perspectives. In *Silicon Photonics and Photonic Integrated Circuits III*; International Society for Optics and Photonics: Bellingham, WA, USA, 2012; Volume 8431, p. 84311D.
3. Boes, A.; Corcoran, B.; Chang, L.; Bowers, J.; Mitchell, A. Status and Potential of Lithium Niobate on Insulator (LNOI) for Photonic Integrated Circuits. *Laser Photon. Rev.* **2018**, *12*, 1700256. [[CrossRef](#)]
4. Rabiei, P.; Gunter, P. Optical and electro-optical properties of submicrometer lithium niobate slab waveguides prepared by crystal ion slicing and wafer bonding. *Appl. Phys. Lett.* **2004**, *85*, 4603–4605. [[CrossRef](#)]
5. Wang, C.; Zhang, M.; Stern, B.; Lipson, M.; Lončar, M. Nanophotonic lithium niobate electro-optic modulators. *Opt. Express* **2018**, *26*, 1547–1555. [[CrossRef](#)] [[PubMed](#)]
6. Saravi, S.; Pertsch, T.; Setzpfandt, F. Lithium Niobate on Insulator: An Emerging Platform for Integrated Quantum Photonics. *Adv. Opt. Mater.* **2021**, *9*, 2100789. [[CrossRef](#)]
7. Hu, H.; Ricken, R.; Sohler, W. Lithium niobate photonic wires. *Opt. Express* **2009**, *17*, 24261–24268. [[CrossRef](#)]

8. Volk, M.F.; Sunstov, S.; Rüter, C.E.; Kip, D. Low loss ridge waveguides in lithium niobate thin films by optical grade diamond blade dicing. *Opt. Express* **2016**, *24*, 1386–1391. [[CrossRef](#)]
9. Courjal, N.; Guichardaz, B.; Ulliac, G.; Rauch, J.-Y.; Sadani, B.; Lu, H.; Bernal, M.-P. High aspect ratio lithium niobate ridge waveguides fabricated by optical grade dicing. *J. Phys. D Appl. Phys.* **2011**, *44*, 305101. [[CrossRef](#)]
10. Cai, L.; Wang, Y.; Hu, H. Low-loss waveguides in a single-crystal lithium niobate thin film. *Opt. Lett.* **2015**, *40*, 3013–3016. [[CrossRef](#)]
11. Rüter, C.E.; Sunstov, S.; Kip, D.; Stone, G.; Dierolf, V.; Hu, H.; Sohler, W. Characterization of diced ridge waveguides in pure and Er-doped lithium-niobate-on-insulator (LNOI) substrates. *Opt. Compon. Mater. XI* **2014**, 8982, 89821G. [[CrossRef](#)]
12. Wang, M.K.; Li, J.H.; Chen, K.; Hu, Z. Thin-film lithium niobate electro-optic modulator on a D-shaped fiber. *Opt. Express* **2020**, *28*, 21464. [[CrossRef](#)]
13. Yu, Z.; Sun, X. Acousto-optic modulation of photonic bound state in the continuum. *Light. Sci. Appl.* **2020**, *9*, 1–9. [[CrossRef](#)] [[PubMed](#)]
14. Mu, B.; Wu, X.; Niu, Y.; Chen, Y.; Cai, X.; Gong, Y.; Xie, Z.; Hu, X.; Zhu, S. Locally periodically poled LNOI ridge waveguide for second harmonic generation [Invited]. *Chin. Opt. Lett.* **2021**, *19*, 060007. [[CrossRef](#)]
15. Wang, C.; Langrock, C.; Marandi, A.; Jankowski, M.; Zhang, M.; Desiatov, B.; Fejer, M.M.; Lončar, M. Ultrahigh-efficiency wavelength conversion in nanophotonic periodically poled lithium niobate waveguides. *Optica* **2018**, *5*, 1438–1441. [[CrossRef](#)]
16. Liu, S.; Zheng, Y.; Fang, Z.; Ye, X.; Cheng, Y.; Chen, X. Effective four-wave mixing in the lithium niobate on insulator microdisk by cascading quadratic processes. *Opt. Lett.* **2019**, *44*, 1456–1459. [[CrossRef](#)] [[PubMed](#)]
17. Zhang, L.; Zheng, D.; Li, W.; Bo, F.; Gao, F.; Kong, Y.; Zhang, G.; Xu, J. Microdisk resonators with lithium-niobate film on silicon substrate. *Opt. Express* **2019**, *27*, 33662–33669. [[CrossRef](#)] [[PubMed](#)]
18. Zhou, Z.; Zhang, S. Electro-optically tunable racetrack dual microring resonator with a high quality factor based on a Lithium Niobate-on-insulator. *Opt. Commun.* **2019**, *458*, 124718. [[CrossRef](#)]
19. Luo, R.; He, Y.; Liang, H.; Li, M.; Ling, J.; Lin, Q. Optical Parametric Generation in a Lithium Niobate Microring with Modal Phase Matching. *Phys. Rev. Appl.* **2019**, *11*, 034026. [[CrossRef](#)]
20. Krasnokutskaja, I.; Chapman, R.J.; Tambasco, J.-L.J.; Peruzzo, A. High coupling efficiency grating couplers on lithium niobate on insulator. *Opt. Express* **2019**, *27*, 17681–17685. [[CrossRef](#)]
21. Chen, Z.; Peng, R.; Wang, Y.; Zhu, H.; Hu, H. Grating coupler on lithium niobate thin film waveguide with a metal bottom reflector. *Opt. Mater. Express* **2017**, *7*, 4010–4017. [[CrossRef](#)]
22. Cai, L.; Piazza, G. Low-loss chirped grating for vertical light coupling in lithium niobate on insulator. *J. Opt.* **2019**, *21*, 065801. [[CrossRef](#)]
23. Hum, D.S.; Fejer, M.M. Quasi-phaseshifting. *Comptes Rendus. Phys.* **2007**, *8*, 180–198. [[CrossRef](#)]
24. Byer, R.L. Quasi-Phase-matched Nonlinear Interactions and Devices. *J. Nonlinear Opt. Phys. Mater.* **1997**, *6*, 549–592. [[CrossRef](#)]
25. Myers, L.E.; Eckardt, R.C.; Fejer, M.M.; Byer, R.L.; Bosenberg, W.R.; Pierce, J.W. Quasi-phase-matched optical parametric oscillators in bulk periodically poled LiNbO₃. *J. Opt. Soc. Am. B* **1995**, *12*, 2102–2116. [[CrossRef](#)]
26. Zhao, J.; Rüsing, M.; Roeper, M.; Eng, L.M.; Mookherjee, S. Poling thin-film x-cut lithium niobate for quasi-phase matching with sub-micrometer periodicity. *J. Appl. Phys.* **2020**, *127*, 193104. [[CrossRef](#)]
27. Niu, Y.; Lin, C.; Liu, X.; Chen, Y.; Hu, X.; Zhang, Y.; Cai, X.; Gong, Y.-X.; Xie, Z.; Zhu, S. Optimizing the efficiency of a periodically poled LNOI waveguide using in situ monitoring of the ferroelectric domains. *Appl. Phys. Lett.* **2020**, *116*, 101104. [[CrossRef](#)]
28. Li, G.; Chen, Y.; Jiang, H.; Chen, X. Broadband sum-frequency generation using d_{33} in periodically poled LiNbO₃ thin film in the telecommunications band. *Opt. Lett.* **2017**, *42*, 939–942. [[CrossRef](#)]
29. Harris, S.E. Proposed backward wave oscillation in the infrared. *Appl. Phys. Lett.* **1966**, *9*, 114–116. [[CrossRef](#)]
30. Slautin, B.; Zhu, H.; Shur, V.Y. Submicron periodical poling by local switching in ion sliced lithium niobate thin films with a dielectric layer. *Ceram. Int.* **2021**, *47*, 32900–32904. [[CrossRef](#)]
31. Slautin, B.N.; Zhu, H.; Shur, V.Y. Submicron periodical poling in Z-cut lithium niobate thin films. *Ferroelectrics* **2021**, *576*, 119–128. [[CrossRef](#)]
32. Volk, T.R.; Gainutdinov, R.V.; Zhang, H.H. Domain-wall conduction in AFM-written domain patterns in ion-sliced LiNbO₃ films. *Appl. Phys. Lett.* **2017**, *110*, 132905. [[CrossRef](#)]
33. Slautin, B.N.; Turygin, A.P.; Greshnyakov, E.D.; Akhmatkhanov, A.R.; Zhu, H.; Shur, V.Y. Domain structure formation by local switching in the ion sliced lithium niobate thin films. *Appl. Phys. Lett.* **2020**, *116*, 152904. [[CrossRef](#)]
34. Volk, T.; Gainutdinov, R.; Zhang, H. Domain Patterning in Ion-Sliced LiNbO₃ Films by Atomic Force Microscopy. *Crystals* **2017**, *7*, 137. [[CrossRef](#)]
35. Gainutdinov, R.V.; Volk, T.R.; Zhang, H.H. Domain formation and polarization reversal under atomic force microscopy-tip voltages in ion-sliced LiNbO₃ films on SiO₂/LiNbO₃ substrates. *Appl. Phys. Lett.* **2015**, *107*, 162903. [[CrossRef](#)]
36. Zhang, L.; Geng, W.; Chen, X.; Li, Y.; Qiao, X.; Hou, X.; He, J.; Mu, J.; Yang, Y.; Chou, X. Enhancing the thermal stability of switched domains in lithium niobate single-crystal thin films. *Ceram. Int.* **2019**, *46*, 9192–9197. [[CrossRef](#)]
37. Jiao, Y.; Shao, Z.; Li, S.; Wang, X.; Bo, F.; Xu, J.; Zhang, G. Improvement on Thermal Stability of Nano-Domains in Lithium Niobate Thin Films. *Crystals* **2020**, *10*, 74. [[CrossRef](#)]
38. Zhang, H.; Zhu, H.; Li, Q.; Hu, H. Reversed domains in x-cut lithium niobate thin films. *Opt. Mater.* **2020**, *109*, 110364. [[CrossRef](#)]

39. Johann, F.; Ying, Y.J.; Jungk, T.; Hoffmann, Á.; Sones, C.L.; Eason, R.W.; Mailis, S.; Soergel, E. Depth resolution of piezoresponse force microscopy. *Appl. Phys. Lett.* **2009**, *94*, 172904. [[CrossRef](#)]
40. Goldstein, J.I.; Newbury, D.E.; Michael, J.R.; Ritchie, N.W.M.; Scott, J.H.J.; Joy, D.C. *Scanning Electron Microscopy and X-ray Microanalysis*, 4th ed.; Springer: New York, NY, USA, 2018.
41. Farooq, M.U.; Villaurrutia, R.; MacLaren, I.; Burnett, T.L.; Comyn, T.P.; Bell, A.J.; Kungl, H.; Hoffmann, M.J. Electron backscatter diffraction mapping of herringbone domain structures in tetragonal piezoelectrics. *J. Appl. Phys.* **2008**, *104*, 024111. [[CrossRef](#)]
42. Burch, M.; Fancher, C.; Patala, S.; De Graef, M.; Dickey, E. Mapping 180° polar domains using electron backscatter diffraction and dynamical scattering simulations. *Ultramicroscopy* **2017**, *173*, 47–51. [[CrossRef](#)]
43. Alikin, D.O.; Ievlev, A.V.; Turygin, A.P.; Lobov, A.I.; Kalinin, S.; Shur, V. Tip-induced domain growth on the non-polar cuts of lithium niobate single-crystals. *Appl. Phys. Lett.* **2015**, *106*, 182902. [[CrossRef](#)]
44. Alikin, Y.M.; Turygin, A.P.; Alikin, D.O.; Shur, V.Y. Tilt control of the charged domain walls created by local switching on the non-polar cut of MgO doped lithium niobate single crystals. *Ferroelectrics* **2021**, *574*, 16–22. [[CrossRef](#)]
45. Eliseev, E.A.; Morozovska, A.N.; Svechnikov, G.S.; Gopalan, V.; Shur, V.Y. Static conductivity of charged domain walls in uniaxial ferroelectric semiconductors. *Phys. Rev. B* **2011**, *83*, 235313. [[CrossRef](#)]
46. Schröder, M.; Haußmann, A.; Thiessen, A.; Soergel, E.; Woike, T.; Eng, L.M. Conducting Domain Walls in Lithium Niobate Single Crystals. *Adv. Funct. Mater.* **2012**, *22*, 3936–3944. [[CrossRef](#)]
47. Esin, A.; Akhmatkhanov, A.; Shur, V. The electronic conductivity in single crystals of lithium niobate and lithium tantalate family. *Ferroelectrics* **2016**, *496*, 102–109. [[CrossRef](#)]
48. McConville, J.P.V.; Lu, H.; Wang, B.; Tan, Y.; Cochard, C.; Conroy, M.; Moore, K.; Harvey, A.; Bangert, U.; Chen, L.; et al. Ferroelectric Domain Wall Memristor. *Adv. Funct. Mater.* **2020**, *30*, 2000109. [[CrossRef](#)]
49. Esin, A.A.; Akhmatkhanov, A.R.; Shur, V.Y. Tilt control of the charged domain walls in lithium niobate. *Appl. Phys. Lett.* **2019**, *114*, 092901. [[CrossRef](#)]
50. Weeks, B.L.; Vaughn, M.W.; DeYoreo, J.J. Direct Imaging of Meniscus Formation in Atomic Force Microscopy Using Environmental Scanning Electron Microscopy. *Langmuir* **2005**, *21*, 8096–8098. [[CrossRef](#)]
51. Shur, V.; Akhmatkhanov, A.R.; Baturin, I. Micro- and nano-domain engineering in lithium niobate. *Appl. Phys. Rev.* **2015**, *2*, 040604. [[CrossRef](#)]
52. Turygin, A.; Alikin, D.; Alikin, Y.; Shur, V. The Formation of Self-Organized Domain Structures at Non-Polar Cuts of Lithium Niobate as a Result of Local Switching by an SPM Tip. *Materials* **2017**, *10*, 1143. [[CrossRef](#)]
53. Ievlev, A.; Jesse, S.; Morozovska, A.N.; Strelcov, E.; Eliseev, E.; Pershin, Y.V.; Kumar, A.; Shur, V.Y.; Kalinin, S. Intermittency, quasiperiodicity and chaos in probe-induced ferroelectric domain switching. *Nat. Phys.* **2013**, *10*, 59–66. [[CrossRef](#)]
54. Turygin, A.P.; Alikin, Y.M.; Neradovskaia, E.A.; Alikin, D.; Shur, V.Y. Self-organized domain formation by moving the biased SPM tip. *Ferroelectrics* **2019**, *542*, 70–76. [[CrossRef](#)]